Article

Hierarchical Cube-in-Cube Cobalt−Molybdenum Phosphide Hollow Nanoboxes Derived from the MOF Template Strategy for High-Performance Supercapacitors

Fatemeh Heidari Gourji,* Tharmakularasa Rajaramanan, Amruthaa Kishore, Marte Heggertveit, and Dhayalan Velauthapillai*

Read Online

| ACCESS | Metrics & More | Article Recommendations | SI Supporting Information |

ABSTRACT: The design of hierarchical hollow nanostructures with complex shell architectures is an attractive and effective way to obtain a desirable electrode material for energy storage application. Herein, we report an effective metal−organic framework (MOF) template-engaged method to synthesize novel double-shelled hollow nanoboxes, in terms of chemical composition and structure complexity, for supercapacitor application. Starting from cobalt-based zeolitic imidazolate framework (ZIF-67(Co)) nanoboxes as the removal template, we developed a rational preparation approach to synthesize cobalt−molybdenum−phosphide (CoMoP) double-shelled hollow nanoboxes (donated as CoMoP-DSHNBs) through (i) ion-exchange reaction, (ii) template etching, and (iii) phosphorization treatment, respectively. Notably, despite the previously reported works, the phosphorization was simply done using the facile solvothermal method, without employing annealing and high-temperature conditions, which can be considered as one of the merits of the current work. CoMoP-DSHNBs showed excellent electrochemical properties owing to their unique morphology, high surface area, and optimal elemental composition. In a three-electrode system, the target material showed a superior specific capacity of 1204 F g^{-1} at 1 A g^{-1} with a remarkable cycle stability of 87% after 20000 cycles. The hybrid device formed of activated carbon (AC) as the negative electrode and CoMoP-DSHNBs as the positive electrode exhibited a high specific energy density of 49.99 W h kg^{-1} and a maximum power density of 7539.41 W kg^{-1} with a great cycling stability of 84.5% after 20,000 cycles.
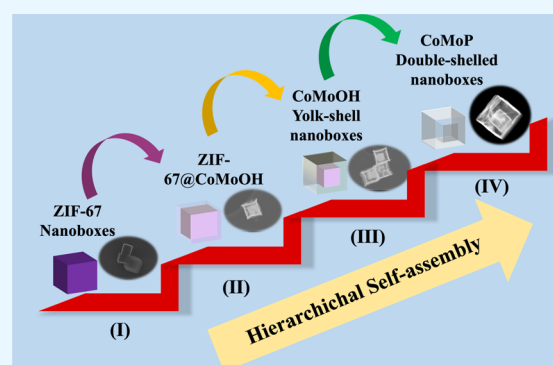
1. INTRODUCTION

To date, fossil fuels, as the nonrenewable and main world's energy supply, have had serious influence on our environment and economy, and hence, development of societies has been highly dependent on it.[1] Therefore, tremendous research efforts are ongoing to develop renewable and sustainable energy storage and conversion technologies.[2,3] Supercapacitors (SCs), as the promising energy storage systems, which bridge the gap between conventional capacitors and batteries, have received significant attention due to their multiple advantages such as high power density, fast charge−discharge rate, and stable cyclability.[4] Nevertheless, low energy density of SCs compared to batteries limits their widespread commercial application.[5] Thus, it is very important to boost the energy density of SCs without compromising high power capability and cyclability.[2,5] One of the most effective approaches to tackle this issue is to design an electrode material with high electrochemical performance. As a result, the rational design of suitable nano/microstructures with engineered content plays an important role to obtain superior capacitive perform-ance.[2,6−8]

Hollow nano/micro-sized particles are of great interest due to their distinctive structure-dependent features and promising applications in many areas. Preparation of hollow structures requires the growth of a desirable shell through the assistance of removable template particles.[9] Moreover, to increase the desirable functionalities of a hollow structure, extensive research efforts have been devoted to design and fabricate complex hollow structures with tunable chemical composition and multiple layers of shells.[9,10] Particularly, multishelled hollow structures are beneficial to enhance the specific surface area, internal space, contact areas of an electrode/electrolyte and can also shorten the diffusion path for electrons, and thus, they can result in fast faradic redox reactions.[11,12] Furthermore,
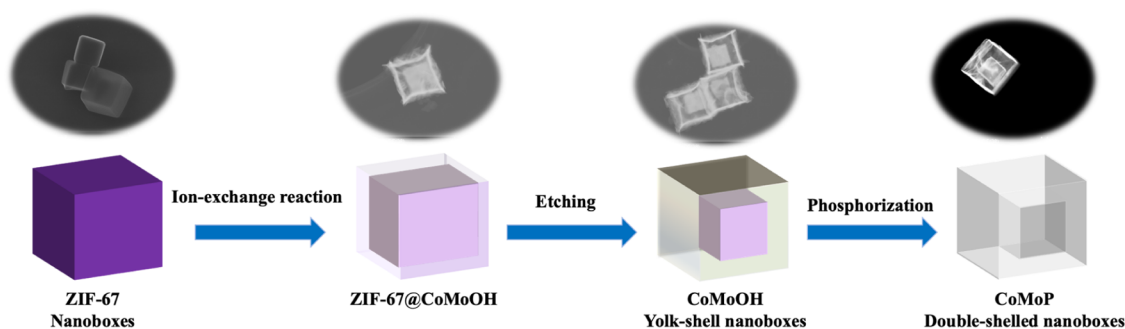
Figure 1. Schematic representation of the preparation process for hierarchical CoMoP double-shelled hollow nanoboxes (CoMoP-DSHNBs).

due to the higher content of active sites in multishelled hollow structures, the energy density would improve significantly.[5]

To fabricate multishelled hollow structures, an effective approach is to employ templating methods, in which assembling of designed materials is well controlled on different sacrificial templates, such as emulsion micelles and mono-disperse silica/polymer latex spheres. However, these type of templating strategies practically have some difficulties, including tedious procedure and incompatibility of desired materials and template surfaces.[9] As such, choosing appropriate templates should be the key point of preparing the complex hollow structures.[6,9] Metal–organic frameworks (MOFs), as a new kind of hybrid porous, crystalline materials consisting of metal ions and organic ligands, have been widely utilized in different fields such as imaging, sensing, gas storage/separation, drug delivery, energy storage, and catalysis.[4,6,11,13] Their interesting properties, such as tailorable architecture, diversity of applicable metals and organic linkers, high porosity, and large specific surface area, make these materials one of the main research targets for different applications during the past decades.[14,15] With respect to prepare hollow structures, MOFs can be considered as both metal precursors and removable templates for preparing well-defined MOF-derived hollow structure materials.[16] The diversity of MOFs with different sizes and shapes has widened their applicability as a choice of templates.[17] The zeolitic imidazolate framework (ZIF), as an example of a typical class of MOFs, shows exceptionally high thermal stability and robustness and can be employed as both a metal precursor and a sacrificial template to prepare porous hollow nano/microstructures.[6,11,17] For instance, Hu et al.,[5] Du et al.,[6] Jiang et al.,[17] Amiri et al.,[11] and Wang et al.[18] commonly employed Co-based ZIF-67 as the sacrificial template and metal precursor to prepare CoS-NP/CoS-NS DSNBs,[5] NiCoMn−OH,[6] Ni−Co-layered double-hydroxide (LDH) nanocages,[17] CoMoSe$_x$ double-shelled hollow nanocages,[11] and CoNiFeP hollow nanoboxes,[18] respectively, for different electrochemical applications including supercapacitors. Nevertheless, to improve the performance of SCs, not only the materials morphology should be considered as the crucial factor but also the composition of nanomaterials should be regulated in a way that a desirable architecture with high electrical conductivity would obtain. Fabrication of multi-metallic oxides/sulfides/phosphides is an effective strategy to overcome the flaws of low electrical conductivity of electrode-based materials. Particularly, the interaction between different metal ions can effectively modulate the three-dimensional electronic nanostructure, leading to fast transport of ions and charges, more accessible redox sites, and improve the ion-electron transfer kinetics.[16,19]

Transitional metal phosphides/phosphates (TMPs) have received notable attention due to their metallic characteristics, high electrical conductivity, and superb specific capacity.[12,19,20] Specifically, phosphorous as a multivalent nonmetal is considered as one of the well-stablished donor atom in coordination chemistry.[21,22] Hence, a diverse class of phosphides can be formed since phosphorus can react with most of the elements in the periodic table.[21,23] Due to their promising advantages with features such as high electrical and heat conductivity, high chemical and mechanical stability, nontoxicity, and high abundance, it is expected that TMPs could play major roles in the development of high-performance supercapacitors.[21] To date, few bimetallic phosphide materials such as NiCoP hollow nanoboxes,[19] MnCoP hollow nano-cubes,[20] NiCoP/CoP nanosheets,[24] Ni$_{1.4}$Co$_{0.6}$P@C micro-spheres,[25] and Ni$_x$Co$_{1-x}$O/Ni$_y$Co$_{2-y}$P@C hybrides[26] have been investigated for high-performance SCs. However, to the best of our knowledge, there is only one report in which bimetallic molybdenum phosphide was employed as the electrode material for SC application. Specifically, in this work, Chen et al., fabricated hierarchical MOF-derived Mo−CoP@NiFe-layered double-hydroxide (LDH) nanosheets as the electrode-based material for hybrid SCs. The as-prepared material showed a large specific capacitance of 2796 F g^{-1} and a good stability of 79.6% after 8000 cycles in a three-electrode cell. Additionally, the hybrid SC exhibited an energy density of 48.6 W h kg^{-1} and an outstanding 90.6% capacitance retention after 20,000 cycles in a two-electrode setup.[27]

Herein, motivated by all the aforementioned ideas, for the first time, we devolved a facile MOF-derived strategy to prepare CoMoP double-shelled hollow nanoboxes (CoMoP-DSHNBs) for supercapacitor application. The overall design and preparation reaction that leads to formation of double-shelled hollow structures is proposed in Figure 1. First, through the cation-exchange reaction at the interface of Co-based ZIF-67 and Na$_2$MoO$_4$ solution, a thin layer of CoMo hydroxide forms on the surface of ZIF-67 (ZIF-67@Co−MoOH). As the reaction continues, H$^+$ ions, which are generated by the hydrolysis procedure, flow inward to supply the cation-exchange reaction, resulting in the oxidation of Co^{2+} into Co^{3+} ions. Then, the originated Co^{3+} ions, through outward diffusion, co-precipitate with Mo ions on the as-formed CoMo hydroxide layer. If the reaction continues slowly, the entire ZIF-67 nanoboxes will be gradually consumed, accompanied by the growth of CoMoOH shell, meaning that, eventually, well-defined CoMoOH nanoboxes with a large interior cavity will be left behind. However, the elevated temperature quickens the inward and outward diffusion of H$^+$ and Co^{3+} ions, respectively, leading to precipitation of a secondary

CoMoOH layer on the inner core before its complete consumption. In this case, a multishelled or double-shelled structure will be formed. Finally, under a modified solvothermal method, in the presence of $NaH_2PO_2 \cdot H_2O$, as a phosphorous precursor, CoMoOH transforms into CoMoP-DSHNBs.[1,5,9] As expected, due to the well-defined double-shelled porous, multicomponent structure and high surface area, CMP-DSHNBs showed an outstanding specific capacity with a rate capability comparable to the other similar yolk-shelled, multicomponent structures.

2. EXPERIMENTAL SECTION

2.1. Materials and Synthesis. *2.1.1. Chemicals.* All chemicals were provided by Sigma-Aldrich and Merck Cooperation. These include cobalt nitrate hexa hydrate Co $(NO_3)_2 \cdot 6H_2O$, hexadecyltrimethylammonium bromide (CTAB), 2-methylimidazole $(C_4H_6N_2)$, sodium molybdate dihydrate $(Na_2MoO_4 \cdot 2H_2O)$, sodium hypophosphite monohydrate $(NaH_2PO_2 \cdot H_2O)$, potassium hydroxide (KOH), and ethanol (C_2H_5OH).

2.1.2. Synthesis of ZIF-67 Particles. According to a formerly reported method,[5] in a typical procedure, 174 mg of $Co(NO_3)_2 \cdot 6H_2O$ was added to 6 mL of deionized water (DI) containing 3 mg of CTAB. After dissolving, this solution was rapidly injected into 42 mL of aqueous solution with 2724 mg of 2-methylimidazole under vigorous stirring for 20 min at room temperature. The purple particles were collected by centrifugation and washed with ethanol several times, followed by vacuum-drying overnight.

2.1.3. Synthesis of ZIF-67@CoMoOH-YSNB Particles. First, 30 mg of ZIF-67 nanoboxes were dispersed in 20 mL of ethanol for 10 min. Then, the obtained solution was heated at 90 °C under reflux and stirring. After 20 min, 5 mL of an aqueous solution containing 100 mg of $Na_2MoO_4 \cdot 2H_2O$ was added to the above solution. The resulting mixture was kept under the reflux at 90 °C for more than 2 h. Then, the product was washed with ethanol several times and dried at 70 °C overnight.

2.1.4. Synthesis of CoMoOH-YSNB Particles. Double-shelled CoMo hydroxide nanoboxes were obtained in sequential steps. First, 50 mg of the ZIF-67@CoMoOH nanoboxes was dispersed in 10 mL of DI. Next, the solution was heated at 90 °C for 15 min, followed by adding a mixture of 5 ml ethanol and 5 mL DMF. The reaction continued for an additional 2 h, until the color disappeared. Then, the product was washed by ethanol several times and dried at 70 °C overnight.

2.1.5. Synthesis of CoMoP-DSHNB Particles. The CoMoP double-shelled hollow nanoboxes were prepared by reaction of CoMo OH yolk-shelled nanoboxes with $NaH_2PO_2 \cdot H_2O$. In a typical synthesis, the obtained CoMoOH yolk-shelled particles were dispersed in 10 mL of ethanol, followed by stirring for 10 min. Then, 5 mL of an aqueous solution containing 230 mg of $NaH_2PO_2 \cdot H_2O$ was added to the above solution, and the mixture was transferred into a Teflon-lined stainless steel autoclave and further heated at 140 °C for another 6 h. The product was collected by centrifugation and washed sequentially with ethanol and water before vacuum-drying overnight.

2.2. Materials Characterization. The crystal structure of the samples was studied through a D8 ADVANCE ECO in a 1 kW copper X-ray tube diffractometer (XRD). The morphology and chemical compositions of the samples were investigated by a scanning electron microscope (FESEM, Jeol JSM-7400F)

attached with an energy-dispersive X-ray (EDX) spectrometer. Scanning transmission electron microscopy (STEM) images were taken on an in-lens cold field SU9000 emission microscope. The surface electron state of the samples was characterized by X-ray photoelectron spectroscopy (XPS, Kratos Axix ultra DLD). The Brunauer–Emmett–Teller (BET) model (Micromeritics Tristar 3000, at 77 K) was employed to determine the specific surface area. Pore size distribution of the samples was measured through the desorption branch of the nitrogen isotherm via the Barrett–Joyner–Halen da (BJH) model.

2.3. Electrochemical Measurement. The electrochemical performance of the as-prepared samples was studied through a SP-150 electrochemical workstation (Biologic Science Instruments) with a three-electrode setup. In this setup, Ag/AgCl (KCl saturated) and Pt electrodes were employed as a reference electrode and counter electrode, respectively, in a 3 M KOH. The working electrode preparation is as follows: 85% of the active material was mixed with 10% of activated carbon (AC) as the conductive agent and 5% of polyvinylidene fluoride as a binder (PVDF) in *N*-methyl-2-pyrrolidinone (NMP) solvent to form a slurry paste. Then, the prepared slurry was coated on a 2 × 1 cm Ni foam as the current collector and was placed in a vacuum oven at 80 °C overnight to evaporate the solvent. The total mass weight of all working electrodes was about ∼3 mg after drying. Cyclic voltammetry (CV) was measured in the potential range of −0.1−0.55 V at different scan rates (10, 20, 30, 50, and 80 mV s^{-1}). For galvanostatic charge−discharge (GCD) measurement, different current densities (1, 2, 4, 6, 8, 10, and 20 A g^{-1}) were recorded. Electrochemical impedance spectroscopy (EIS) measurements were conducted in the frequency range of 100 Hz−100 kHz. The specific storage capacities were calculated using the GCD curves from the following equation[28]

$$C_m = I \times \Delta t / m \times \Delta V (\text{F g}^{-1}) \qquad (1)$$

where m is the total loaded mass of the active material in mg, Δt is the discharge time in s, I is the discharge current in A, and ΔV is the working potential window in V. The specific storage capacitance can also be measured in mA h g^{-1} based on the following formulas[28]

Specific capacitance from the CV plot: C

$$= \int I \times \mathrm{d}v / 2 \times 3.6 \times m \times v (\text{mA h g}^{-1}) \qquad (2)$$

Specific capacitance from the GCD plot: C

$$= I \times \Delta t / 3.6 \times m (\text{mA h g}^{-1}) \qquad (3)$$

where $\int I \times \mathrm{d}v$ is the CV curve area, Δt is the discharge time in s, I is the discharge current in A, m is the total mass of active material in mg, and v is the scanning rate in mV s^{-1}.

2.3.1. Fabrication of an Asymmetric Supercapacitor Device. In a two-electrode setup (CoMoP-DSHNBs (+)//AC (−)), the device was fabricated by employing CMP-DSHNBs as the positive electrode and AC as the negative electrode, in which the two electrodes were separated by cellulose paper and 3 M KOH used as an electrolyte. The optimal mass ratio (m_+/m_-) of the asymmetric supercapacitor device (ASC) device was calculated according to the charge balance theory employing the following equation
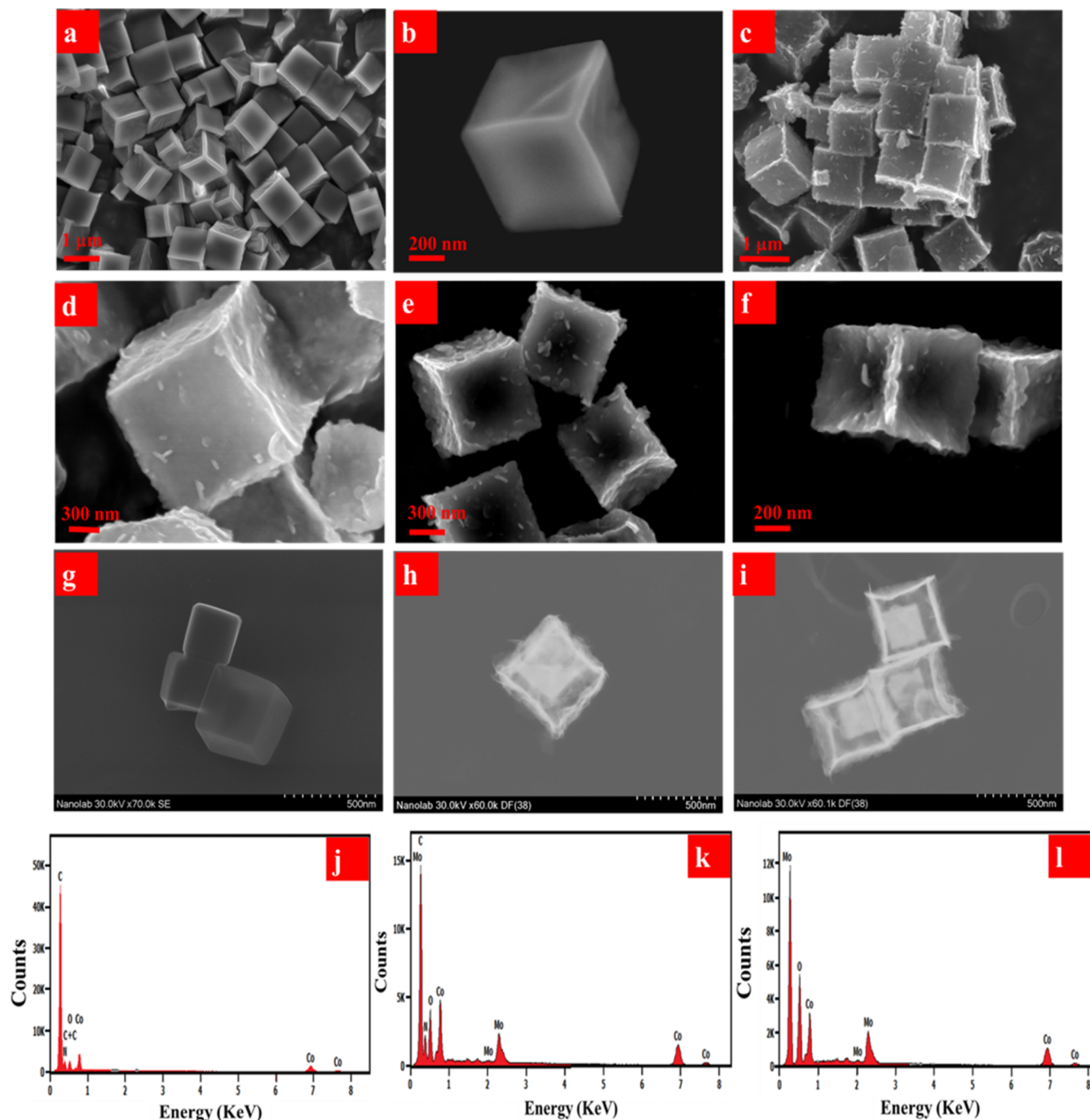
Figure 2. FESEM images of ZIF-67 particles (a,b), ZIF-67@CoMoOH-YSNBs (c,d), and CoMoOH-YSNBx (e,f); STEM images of ZIF-67 particles (g), ZIF-67@CoMoOH-YSNBs (h), and CoMoOH-YSNBx (i); and EDX spectra of ZIF-67 particles (j), ZIF-67@CoMoOH-YSNBs (k), and CoMoOH-YSNBx (l).

$$\frac{m_+}{m_-} = \frac{C_- \times \Delta V_-}{C_+ \times \Delta V_+} \tag{4}$$

where C_-/C_+ shows the ratio of specific capacitances and $\Delta V_-/\Delta V_+$ displays the ratio of potential ranges for the anode ($-$) and cathode materials ($+$), respectively. The energy density (E) and power density (P) of the solid-state electrode device were, then, calculated according to equations 5 and 6, respectively[29,30]

$$E = \frac{C \times \Delta V^2}{7.2} (\text{W h kg}^1) \tag{5}$$

$$P = 3600 \times E/\Delta t (\text{W kg}^{-1}) \tag{6}$$

where E is the specific energy in W h kg^{-1}, C is the specific capacitance of the solid-state device in F g^{-1}, ΔV is the working potential window in V, P is the power density in W kg^{-1}, and Δt is the discharge time in s.

3. RESULTS AND DISCUSSION

3.1. Morphology and Structure. To observe the morphology of the samples, field-emission scanning electron microscopy (FESEM) images of the prepared samples were conducted. As shown in Figure 2a,b, the ZIF-67 nanoparticles
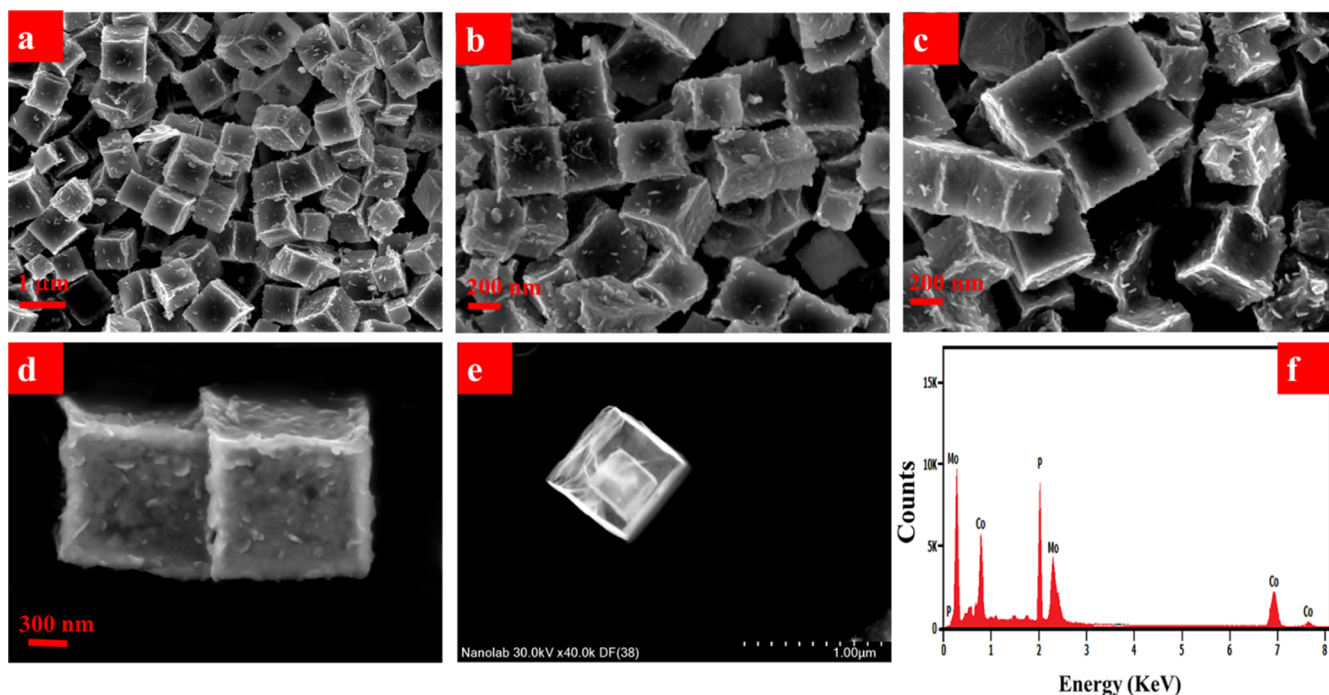
Figure 3. FESEM images of CoMoP-DSHNBx (a,b,c,d), STEM images of CoMoP-DSHNBx (e), and EDX spectra of CoMoP-DSHNBx (f).
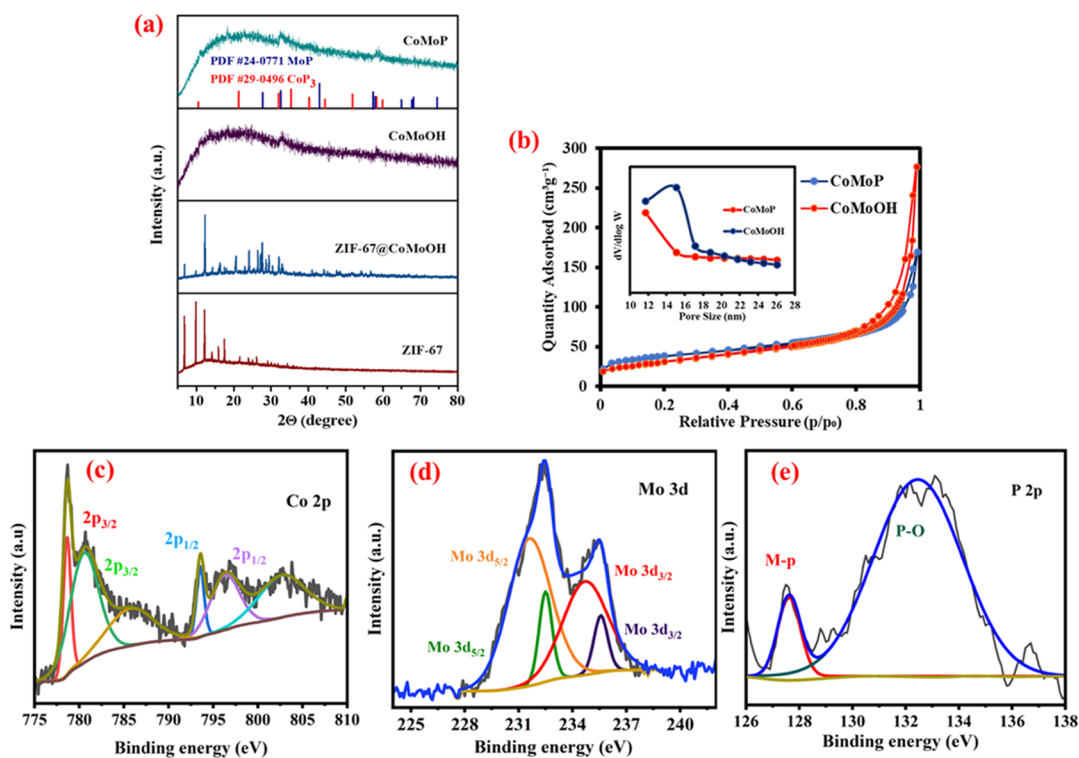

Figure 4. XRD pattern of ZIF-67, ZIF-67@CoMoOH-YSNBs, CoMoOH-YSNBs, and CoMoP-DSHNBs (a) and N2 adsorption−desorption isotherm loops of CoMoOH-YSNBs and CoMoP-DSHNBs, and the inset is the pore size distribution curves of CoMoOH-YSNBs and CoMoP-DSHNBs (b). High-resolution XPS spectra of Co 2p (c), Mo 3d (d), and P 2p (e) of CoMoP-DSHNBs.

have a well-defined cube-like morphology with smooth surface, in which the size of the particles is uniformly distributed. Furthermore, the prepared particles showed uniform contrast under scanning transmission electron microscopy (STEM) (Figure 2g), revealing their solid nature.[5] These observations are in good agreement with the previous reports.[5,31] After being exchanged by MoO_4^{-2} ions and chemical etching, the

obtained ZIF-67@CoMoOH yolk-shelled nanoboxes still maintain the cubic structure while their surface becomes rough because of the formation of a new exterior shell layer on the ZIF-67 surface (Figure 2c,d,h). Further, in the third stage of the reaction, through the heat treatment, the surface of nanoboxes started to shrink significantly, which might have resulted from the removal of 2-Mlm and CTAB. The STEM
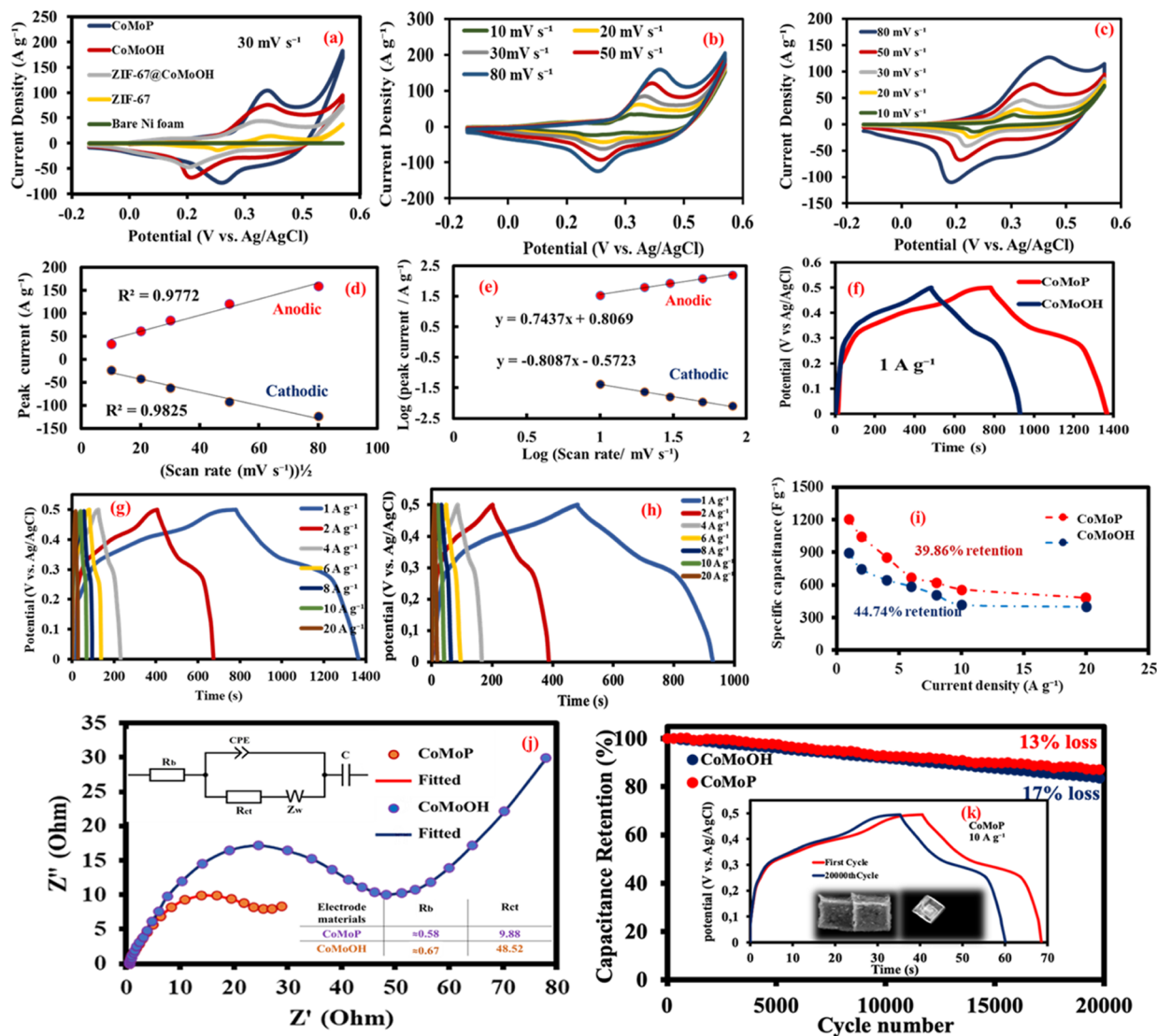
Figure 5. Electrochemical characterization of the as-prepared samples in a three-electrode setup. CV curves of the bare Ni foam, ZIF-67 nanoboxes, ZIF-67@CoMoOH-YSNB electrode, CoMoOH-YSNB electrode, and CoMoP-DSHNB electrode at a scan rate of 30 mV s^{-1} in a 3.0 M KOH electrolyte (a); CV curves of the CoMoOH-YSNB electrode at different scan rates in a 3.0 M KOH electrolyte (b); CV curves of the CoMoP DSHNB electrode at different scan rates in a 3.0 M KOH electrolyte (c); linear plots of anodic/cathodic peak current as a function of square root of scan rate (d); linear plots of logarithm of peak currents as a function of the logarithm of scan rates (e); GCD curves of CoMoOH-YSNB and CoMoP-DSHNB electrodes at 1 A g^{-1} (f); GCD curves of CoMoP-DSHNBs at different current densities (g); GCD curves of CoMoOH-YSNBs at different current densities (h); rate capability of CoMoOH-YSNB and CoMoP-DSHNB electrodes (i); Nyquist plots of CoMoOH-YSNB and CoMoP-DSHNB electrodes (j); and stability retention of CoMoOH-YSNB and CoMoP-DSHNB electrodes at a current density of 10 A g^{-1} (k).

images also revealed the yolk-shelled structure of cube-like CoMoOH particles (Figure 2i) in this stage.

Finally, after phosphorization with NaH$_2$PO$_2$·H$_2$O at 85 °C, the crystalline CoMoP nanoboxes were converted into CoMoP double-shelled hollow nanoboxes. The overall morphology of the synthesized sample as indicated in FESEM images (Figure 3a−d) are much rougher compared to the pervious stages, while the hierarchical cubic structure was well retained without any aggregation. As elucidated by STEM (Figure 3e) observation, both the presence of void space and structure can be verified. Specifically, it can clearly be seen that both inner and exterior shells display a cubic shape.

The EDX spectra of the samples after each synthesis stage were recorded. From the ZIF-67 spectra (Figure 2j), the presence of Co, C, N, and O with the atomic percentages of 12.45, 45.08, 16.74, and 24.65, respectively, can be confirmed.

The EDX spectrum of ZIF-67@CoMoOH-YSNBs (Figure 2k) verified the existence of Co, Mo, C, N, and O elements, and their atomic percentages were 25.79, 41.77, 7.95, 1.74, and 22.75, respectively. EDX analysis of CoMoOH-DSYNBs (Figure 2l) with the atomic percentage of 37.57 for Co, 52.15 for Mo, and 10.28 for O was performed. Meanwhile, the obtained EDX spectrum for CoMoP-DSHNBs (Figure 3f) approved the presence of P with the atomic percentage of 38.10 along with Co (15.78) and Mo (46.11).

Figure 4a displays the crystalline phases of the synthesized samples, obtained from XRD analysis. The diffraction peaks of the ZIF-67 template are in good accordance with the previously reported patterns, confirming that the as-prepared templates are phase pure.[5,31] The XRD patterns of ZIF-67@ CoMoOH show distinct diffraction peaks, suggesting that the MOF core is not completely etched. The relatively low peak

intensity in the diffraction peaks of CoMoOH-YSNBs after stage 3 can be associated with the decomposition of the ZIF-67 template, which was already confirmed through EDX analysis. Eventually, as the crystal phase of CoMoP-DSHNBs investigated, the obtained diffraction peaks can be well indexed to CoP_3 (PDF no. 29−0496) and MoP (PDF no. 24−0771). The peaks at 11.3, 21.3, 32.07, 35.1, 40.1, 44.5, 51.6, 58.1, and 59.9° represent the cubic structure of CoP_3, while the diffraction peaks at 2θ values of 27.8, 32.7, 42.9, 57.3, 64.8, 67.7, 68.04, and 74.4° correspond to the hexagonal planes of MoP.[32,33]

3.2. Surface Area Analysis.
The specific surface area and pore size distribution of the as-obtained samples were evaluated through the BET and BJH measurements, and the results are represented in Figure 4b. As shown in Figure 4b, both CoMoOH-YSNBs and CoMoP-DSHNBs samples reveal the typical type-IV Langmuir N_2 adsorption−desorption isotherm. The BET surface areas of CoMoOH-YSNBs and CoMoP-DSHNBs are estimated to be 128.697 and 111.055 m^2 g^{-1}, respectively, which verify their porous structure and numerous active sites for enhanced electrochemical performance of the electrode. Moreover, the pore size distribution of both samples is in the mesoporous range (∼12−26 nm) (inset plot in Figure 4b), which were measured by BJH techniques.

3.3. Surface Elements Characterization.
To further survey the surface electronic state and elemental composition of CoMoP-DSHNBs, the XPS analysis was performed, and the results are presented in Figure 4c−e. From the XPS spectra of Co 2p (Figure 4c), the peaks positioned at 781 and 795 eV are assigned to Co^{2+}, while the peaks at 779 and 794 eV are the characteristic peaks of Co^{3+}.[34] The obtained result for the Mo 3d spectrum (Figure 4d) displays two characteristic peaks at 231 and 234 eV attributed to Mo $3d_{3/2}$ and $3d_{5/2}$ of CoMoP, respectively, related to Mo^{4+}. The two other fitting peaks at 232 and 236 eV are related to Mo $3d_{5/2}$ and Mo $3d_{3/2}$ of Mo^{+5}.[11] The P 2p XPS spectrum shows the main peaks around 127 eV assigned to metal-P bonds (Co and Mo)−P in the reduced form. Moreover, the distinct peak at 132 eV indicates that the P-metal species are oxidized due to the exposure of metal phosphides to the air.[19]

3.4. Electrochemical Performance of the Electrodes.
First, to evaluate the electrochemical performance of the as-prepared samples, a three-electrode setup immersed in 3 M KOH as an aqueous alkaline electrolyte was employed. Figure 5a shows the CV curves of ZIF-67, ZIF-67@CoMoOH, CoMoOH-YSNBs, and CoMoP-DSHNBs at a scan rate of 30 mV s^{-1} in a broad potential range of −0.1−0.55 V (vs Ag/AgCl electrode). All electrodes showing a pair of distinct redox peaks imply the faradaic nature of the materials, in which a reversible redox reaction attributed to Co^{2+}/Co^{3+} and Mo^{4+}/Mo^{5+} happens. Also, as it is evident, the CoMoP-DSHNB electrode compared with other electrodes shows the largest integration area, indicating higher specific capacitance and faster reaction kinetics. This might be as the result of (i) tailored combination of Co−Mo−P composition, (ii) double-shelled hollow morphology, and (iii) enhanced conductivity of CoMoP as discussed elsewhere.[11] It is noteworthy to mention that the Ni foam does not take part in the redox reaction, and hence, it shows a negligible CV area at the same scan rate. The detailed electrochemical process can be described by eqs 7 and 8 as frequently reported in other literature studies[19]

$$CoMoP + 2OH^- \leftrightarrow CoP_{1-x}OH + MoP_xOH + 2e^- \quad (7)$$

$$MoP_xOH + OH^- \leftrightarrow MoP_xO + H_2O + e^- \quad (8)$$
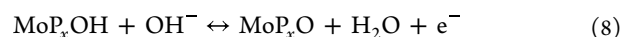
As can be seen in the equations, the coexistence of Co and Mo leads to multiple redox reactions which overlap with each other during the electrochemical process. Figure 5b,c shows the CV curves of CoMoOH-YSNBs and CoMoP-DSHNBs at different scan rates of 10, 20, 30, 50, and 80 mV s^{-1}. As it is evident in both graphs, the integrated CV areas and current densities continuously increase by increasing the scan rates. Furthermore, the shape of the graphs remained unchanged, showing that the target electrode has a desirable rate capability and high reversibility under the fast faradic reaction.[19] Also, the slight shift of the peaks to more a positive and negative potential might be due to the electrode polarization or internal resistance of the electrode materials.[16,19]

To evaluate the charge storage kinetics, calibration curves of oxidative/reductive peak currents (i_p) versus the square root of scan rates (v)$^{1/2}$ were plotted (Figure 5d). Through this calibration curve, the diffusion-controlled charge mechanism of the CoMoP-DSHNB electrode can be calculated. For this aim, the equation of power law was employed

$$\text{Log } i_p = \log a + b\log(v) \quad (9)$$

where i_p is the peak current, v is the scan rate, a is a constant, and b is the power law exponent. The value of b can be calculated from the slope of the linear fit to the curve of log (v) against Log (i_p). $b \sim 1$ indicates that the electrode has a capacitive-type behavior, while $b \sim 0.5$ indicates the battery-type behavior of the electrode. In the plotted graph (Figure 5e), the b values for the anodic and cathodic peaks are 0.7437 and 0.8087, respectively, suggesting that it has a capacitive-type behavior.

Figure 5f exhibits the GCD measurement of CoMoOH-YSNB and CoMoP-DSHNB electrodes at a current density of 1 A g^{-1} in a potential range of 0−0.5 V (vs Ag/AgCl). As can be seen, both curves show a nonlinear GCD behavior, revealing their faradaic redox reaction, which corresponds well with the CV curves. Figure 5g presents the GCD curves of CoMoP-DSHNBs at different current densities including 1, 2, 4, 6, 8, 10, and 20 A g^{-1}. The specific capacitance of 1204, 1048, 856, 672, 624, 560, and 480 F g^{-1} at current densities of 1, 2, 4, 6, 8, 10, and 20 A g^{-1} was obtained. On the contrary, the specific capacitance values calculated for the CoMoOH-YSNB electrode were 894, 748, 647, 588, 512, 420, and 400 F g^{-1} at the same current densities (Figure 5h). The obtained results clearly show that the CoMoP-DSHNB electrode, in comparable applied current densities, has a higher specific capacitance than the CoMoOH-YSNB electrode, which is in good agreement with CV results. Also, it can be concluded that CoMoP-DSHNBs have a higher rate capability compared to CoMoOH-DYSNBs, which is mainly related to the highly porous structure of the double-shelled hollow structure of this material. Due to this desirable morphology, there are more active sites for redox reactions, as well as more efficient pathways for rapid electrolyte diffusion. Additionally, 39.86% of the initial specific capacitance value at a current density of 20 A g^{-1} is preserved as depicted in Figure 5i.

The Nyquist plots of the CoMoOH-YSNB and CoMoP-DSHNB electrodes together with an equivalent circuit diagram are depicted in Figure 5j. As demonstrated in the graphs, the bulk resistance (R_b) of the CoMoOH-YSNB electrode is slightly higher (0.67 Ω) compared to that of the CoMoP-DSHNB electrode (0.58 Ω). The lower R_b of the CoMoP-
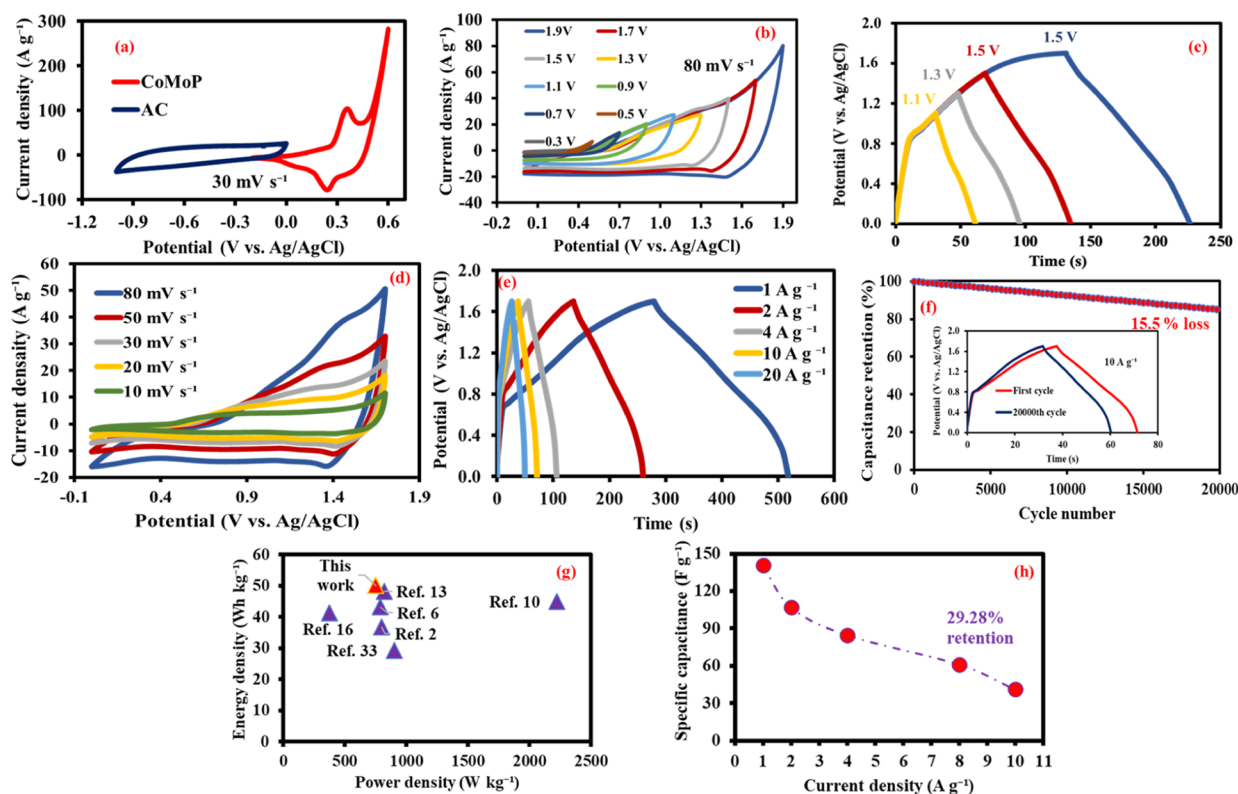
Figure 6. Electrochemical characterization of the CoMoP-DSHNBs (+)//AC (−) asymmetric device. CV curves of AC and CoMoP-DSHNB electrodes at a scan rate of 30 mV s^{-1} in the aqueous 3.0 M KOH electrolyte in a half-cell setup (a), CV curves of a CoMoP-DSHNB (+)//AC (−) asymmetric device at different potential windows (b), GCD curves of a CoMoP-DSHNB (+)//AC (−) asymmetric device at different potential windows and a current density of 3 A g^{-1} (c), CV curves of a CoMoP-DSHNB (+)//AC (−) asymmetric device at different scan rates (d), GCD curves of a CoMoP-DSHNB (+)//AC (−) asymmetric device at different current densities (e), cycling performance of a CoMoP-DSHNB (+)//AC (−) asymmetric device (f), comparison between a CoMoP-DSHNB (+)//AC (−) asymmetric device and other previously reported electrode materials (g), and rate capability of the device (h).

DSHNB electrode confirms the increased conductivity of these electrode materials after phosphating. The bulk resistance, which is also known as internal resistance, is attributed to the total resistance of the bulk electrolyte, electrode, and contact resistance between the electrode and the current collector.[35] The diameter of the semicircle shows the electrolyte resistance in the pores of the electrode or the so-called charge-transfer resistance (R_{ct}).[35] As it is evident, the CoMoOH-YSNB electrode shows a bigger semicircle, implying a higher charge-transfer resistance (48.52 Ω) than CoMoP-DSHNBs (9.88 Ω). The vertical line in the plots is attributed to the Warburg impedance element (W) concerned to the ion diffusion resistance caused by ion diffusion through porous electrodes.[36] According to the plots, CoMoOH-YSNBs shows higher value for ion diffusion resistance, indicating that there is higher limitation for ion transport in the bulk electrolyte and in the porous structure of the electrode.[35]

For further electrochemical assessment of the CoMoOH-YSNB and CoMoP-DSHNB electrodes, the conductivity of these two electrodes was calculated, and the results are depicted in Table S1. According to the obtained results, the CoMoP-DSHNB electrode shows a conductivity of 172.41 S m^{-1}, while this value is 149.25 S m^{-1}, implying that phosphating resulted in superior conductivity of the final material.

As depicted in Figure 5k, the cycling stability test for CoMoOH-YSNB and CoMoP-DSHNB electrodes was conducted by repeating charge−discharge cycles for 20,000th

cycles at a current density of 10 A g^{-1}. Cyclability is one of the main factors to estimate the practical application of electrode materials. As can be seen in Figure 5k, the capacity retention ratio of the CoMoP-DSHNB electrode is 87%, approving its excellent cycling stability, while 84% of the initial capacity for the CoMoOH-YSNB electrode was preserved after 20,000th cycles. This outstanding stability of the electrodes might relate to different reasons, including (i) the unique double-shelled hollow morphology of nanoboxes which alleviate the volume expansion and mechanical strain, (ii) the porosity of the structure shortens the diffusion path of the OH$^-$ ions/ electrons and results in more active sites for faradaic redox reactions at high current densities, and (iii) due to the low electronegativity of phosphorous in the structure and favorable synergetic effect of Co and Mo, the electron transfer accelerates.[19]

3.5. Electrochemical Performance of a CoMoP-DSHNBs (+)//AC (−) Device. To investigate the actual application of the CoMoP-DSHNB electrode, an ASC was fabricated, in which the CoMoP-DSHNB electrode was employed as the positive electrode and AC was utilized as the negative electrode. In Figure 6a, the CV curves of AC and CoMoP-DSHNB electrodes at a scan rate of 30 mV s^{-1} are depicted. Figure 6b shows the CV curves of the asymmetric device at different potential windows at a scan rate of 80 mV s^{-1}. As can be seen, by increasing the potential window up to 1.7 V, the ASC device does not show any polarization and it is very stable. However, when the voltage continues to increase

Table 1. Summary of Electrochemical Performance of Previously Reported Works Compared to This Work

	three-electrode setup		two-electrode setup				
material	specific capacitance at current density	cycle retention	specific capacitance at current density	cycle retention	E (W h Kg^{-1})	P (W Kg^{-1})	ref
Hollow NiCoMn−OH polyhedra	1654.5 F g^{-1} at 1.5 A g^{-1}	70.2%@ 2500	121.5 F g^{-1} at 1 A g^{-1}	100@ 10000	43.2	790	6
NiCoP hollow nanocubes	658 F g^{-1} at 1 A g^{-1}	80.7%@ 5000	133.3 F g^{-1} at 0.5 A g^{-1}	90.8%@ 10000	41.3	373.3	19
CoS2@Ni (OH)2 core−shell nanotube	743 C g^{-1} at 1 A g^{-1}	91.6%@ 3000	64.9 F g^{-1} at 1 A g^{-1}	85.5%@ 3000	29.22	899.2	37
CoMoSex double-shelled hollow nanocage	1029.8 F g^{-1} at 2 A g^{-1}	95.2%@ 8000	125 F g^{-1} at 1 A g^{-1}	94% @ 8000	45	2222	11
hollow-concave CoMoSx boxes	784 F g^{-1} at 1 A g^{-1}	82.5%@ 10000	104.2 F g^{-1} at 1 A g^{-1}	77.6%@ 10000	36.9	800	2
Rugby-ball-like FeCoCuS2	1060 F g^{-1} at 2 A g^{-1}	96.5%@ 7000	133.5 F g^{-1} at 1 A g^{-1}	93.8%@ 7000	48.2	820.1	16
CoMoP double-shelled hollow nanoboxes	1204 F g^{-1} at 1 A g^{-1}	87%@ 20000	103.5 F g^{-1} at 1 A g^{-1}	84%@ 20000	49.99	752.94	this work

to 1.9 V, the CV curve shows a distinct polarization. This is verified by stable and homomorphic GCD curves as illustrated in Figure 6c. Thus, 0−1.7 V was chosen as the potential window of the ASC device and employed in further experimental tests. Figure 6d shows the CV diagrams of the prepared ASC device at different scan rates. As it is evident, the ASC device shows a perfect shape retention with a negligible peak shift. However, in higher scan rates, the curves showed a considerable deviation from rectangular shape, which is associated with the EDLC characteristic of the materials, and they mixed with pseudocapacitive property showing redox faradic peaks, which confirms that the target device possesses both EDLC and faradaic battery-type behavior.

Moreover, the electrochemical performance of the AC as the anode electrode was evaluated, and the obtained CV and GCD results are illustrated in Figure S1. The obtained capacitances at current densities of 1, 2, 4, 10, and 20 A g^{-1} are calculated to be 208, 150, 128, 120, and 104 F g^{-1}, respectively.

Figure 6e displays the GCD curves of the CoMoP-DSHNB (+)//AC (−) device at different current densities. The curves show a symmetrical shape, suggesting superior Columbic efficiency. The calculated specific capacitances of the CoMoP-DSHNBs (+)//AC (−) device from GCD curves were 140, 107.05, 87.12, 70.58, and 41.17 F g^{-1} at current densities of 1, 2, 4, 8, and 10 A g^{-1}, respectively. Furthermore, the device still retains 84.5% of its capacitance at a current density of 10 A g^{-1}, after 20,000th cycles, showing the outstanding cycle stability (Figure 6f). These results are comparable with other similar ASC devices, which are already reported in literature studies (Table 1 and Figure 6g). The fabricated device delivered a great energy density of 49.99 W h kg^{-1} at a high power density of 752.94 W kg^{-1}. Interestingly, the energy density still preserved at 14.64 W h kg^{-1} when the power density increased to 7539.41 W kg^{-1}, showing that the device can maintain 28% of initial capacitance after increasing the current density from 1 to 10 A g^{-1} (Figure 6h). The excellent electrochemical performance of the fabricated devices confirms its potential as a great candidate in energy conversion application.

4. CONCLUSIONS

In conclusion, through an effective and facile template-engaged method, the hierarchical mesoporous CoMoP hollow double-shelled nanocubes (DSHNBs), as an advanced electrode with desirable features, were prepared. Benefiting from the complex hollow morphology and the effective integrated multiple

compositions, the fabricated CoMoP electrode showed a remarkable specific capacity of 1204 F g^{-1} at 1 A g^{-1} with great rate capability and excellent cycle performance (87% after 20,000 cycles at 10 A g^{-1}). Moreover, the CoMoP-DSHNB (+)//AC (−) device delivered a high energy density of 49.99 W h kg^{-1} at a power density of 752.94 W kg^{-1}. The overall electrochemical results clearly suggest that CoMoP would be a promising candidate in energy storage devices.

■ ASSOCIATED CONTENT

ⓢ Supporting Information

The Supporting Information is available free of charge at https://pubs.acs.org/doi/10.1021/acsomega.3c00337.

Calculated conductivity of the CoMoOH-YSNB and CoMoP-DSHNB electrodes and electrochemical data of the AC electrode material (PDF)

■ AUTHOR INFORMATION

Corresponding Authors

Fatemeh Heidari Gourji − *Department of Computer Science, Electrical Engineering and Mathematical Sciences, Western Norway University of Applied Sciences, Bergen 5063, Norway;* ⓞ orcid.org/0000-0002-2510-6990; Phone: +47 55 58 75 91; Email: Fatemeh.Heidari.Gourji@hvl.no

Dhayalan Velauthapillai − *Department of Computer Science, Electrical Engineering and Mathematical Sciences, Western Norway University of Applied Sciences, Bergen 5063, Norway;* ⓞ orcid.org/0000-0002-4162-7446; Phone: +47 55 58 77 11; Email: Dhayalan.Velauthapillai@hvl.no

Authors

Tharmakularasa Rajaramanan − *Department of Computer Science, Electrical Engineering and Mathematical Sciences, Western Norway University of Applied Sciences, Bergen 5063, Norway*

Amruthaa Kishore − *Department of Mechanical and Marine Engineering, Western Norway University of Applied Sciences, Bergen 5063, Norway*

Marte Heggertveit − *Department of Mechanical and Marine Engineering, Western Norway University of Applied Sciences, Bergen 5063, Norway*

Complete contact information is available at:
https://pubs.acs.org/10.1021/acsomega.3c00337

■ REFERENCES

(1) Luo, Q.; Zhao, Y.; Qi, Y.; Xin, H.; Wang, C.; Chen, G.; Sun, J.; Liu, M.; Xu, K.; Ma, F. Plasma-assisted nitrogen doping in Ni−Co−P hollow nanocubes for efficient hydrogen evolution electrocatalysis. *Nanoscale* **2020**, *12*, 13708−13718.

(2) Chen, J.; Zhang, L.; Bai, W.; Zhou, Y.; Li, C.; Guo, T.; Chen, P.; Zhu, J.; Wang, X.; Fu, Y. Unique hollow-concave CoMoSx boxes with abundant mesoporous structure for high-performance hybrid supercapacitors. *Electrochim. Acta* **2020**, *337*, 135824.

(3) Kang, C.; Ma, L.; Chen, Y.; Fu, L.; Hu, Q.; Zhou, C.; Liu, Q. Metal-organic framework derived hollow rod-like NiCoMn ternary metal sulfide for high-performance asymmetric supercapacitors. *Chem. Eng. J.* **2022**, *427*, 131003.

(4) Zhang, Y. Z.; Cheng, T.; Wang, Y.; Lai, W. Y.; Pang, H.; Huang, W. A simple approach to boost capacitance: flexible supercapacitors based on manganese oxides@ MOFs via chemically induced in situ self-transformation. *Adv. Mater.* **2016**, *28*, 5242−5248.

(5) Hu, H.; Guan, B. Y.; Lou, X. W. D. Construction of complex CoS hollow structures with enhanced electrochemical properties for hybrid supercapacitors. *Chem* **2016**, *1*, 102−113.

(6) Du, Y.; Li, G.; Chen, M.; Yang, X.; Ye, L.; Liu, X.; Zhao, L. Hollow nickel-cobalt-manganese hydroxide polyhedra via MOF templates for high-performance quasi-solid-state supercapacitor. *Chem. Eng. J.* **2019**, *378*, 122210.

(7) Guo, H.; Li, T.; Chen, W.; Liu, L.; Qiao, J.; Zhang, J. Self-assembly formation of hollow Ni-Fe-O nanocage architectures by metal-organic frameworks with high-performance lithium storage. *Sci. Rep.* **2015**, *5*, 13310−10.

(8) Chen, L.; Xu, X.; Wan, L.; Zhu, G.; Li, Y.; Lu, T.; Albaqami, M. D.; Pan, L.; Yamauchi, Y. Carbon-incorporated Fe 3 O 4 nanoflakes: high-performance faradaic materials for hybrid capacitive deionization and supercapacitors. *Mater. Chem. Front.* **2021**, *5*, 3480−3488.

(9) Zhang, L.; Wu, H. B.; Lou, X. W. Metal−organic-frameworks-derived general formation of hollow structures with high complexity. *J. Am. Chem. Soc.* **2013**, *135*, 10664−10672.

(10) Shen, L.; Yu, L.; Wu, H. B.; Yu, X.-Y.; Zhang, X.; Lou, X. W. D. Formation of nickel cobalt sulfide ball-in-ball hollow spheres with enhanced electrochemical pseudocapacitive properties. *Nature communications* **2015**, *6*, 6694−6698.

(11) Amiri, M.; Saeed Hosseiny Davarani, S.; Ebrahim Moosavifard, S.; Fu, Y.-Q. Cobalt-molybdenum selenide double-shelled hollow nanocages derived from metal-organic frameworks as high performance electrodes for hybrid supercapacitor. *J. Colloid Interface Sci.* **2022**, *616*, 141−151.

(12) Wang, M.; Zhong, J.; Zhu, Z.; Gao, A.; Yi, F.; Ling, J.; Hao, J.; Shu, D. Hollow NiCoP nanocubes derived from a Prussian blue analogue self-template for high-performance supercapacitors. *J. Alloys Compd.* **2022**, *893*, 162344.

(13) Li, Y.; Zhu, G.; Xu, X.; Chen, L.; Lu, T.; Hill, J. P.; Pan, L.; Yamauchi, Y. Embedding metal−organic frameworks for the design of flexible hybrid supercapacitors by electrospinning: synthesis of highly graphitized carbon nanofibers containing metal oxide nanoparticles. *Small Structures* **2022**, *3*, 2200015.

(14) Yin, D.; Huang, G.; Sun, Q.; Li, Q.; Wang, X.; Yuan, D.; Wang, C.; Wang, L. RGO/Co3O4 composites prepared using GO-MOFs as precursor for advanced lithium-ion batteries and supercapacitors electrodes. *Electrochim. Acta* **2016**, *215*, 410−419.

(15) Xu, X.; Tang, J.; Qian, H.; Hou, S.; Bando, Y.; Hossain, M. S. A.; Pan, L.; Yamauchi, Y. Three-dimensional networked metal−organic frameworks with conductive polypyrrole tubes for flexible supercapacitors. *ACS Appl. Mater. Interfaces* **2017**, *9*, 38737−38744.

(16) Amiri, M.; Moosavifard, S. E.; Hosseiny Davarani, S. S.; Shamsipur, M. Novel Rugby-Ball-like FeCoCuS2 Triple-Shelled Hollow Nanostructures with Enhanced Performance for Super-capattery. *Energy Fuels* **2021**, *35*, 15108−15117.

(17) Jiang, Z.; Li, Z.; Qin, Z.; Sun, H.; Jiao, X.; Chen, D. LDH nanocages synthesized with MOF templates and their high perform-ance as supercapacitors. *Nanoscale* **2013**, *5*, 11770−11775.

(18) Wang, Y.; Sun, L.; Lu, L.; Xu, D.; Hao, Q.; Liu, B. A sequential template strategy toward hierarchical hetero-metal phosphide hollow nanoboxes for electrocatalytic oxygen evolution. *J. Mater. Chem. A* **2021**, *9*, 3482−3491.

(19) Li, P.; Zhang, M.; Yin, H.; Yao, J.; Liu, X.; Chen, S. Hierarchical mesoporous NiCoP hollow nanocubes as efficient and stable electrodes for high-performance hybrid supercapacitor. *Appl. Surf. Sci.* **2021**, *536*, 147751.

(20) Amiri, M.; Moosavifard, S. E.; Davarani, S. S. H.; Kaverlavani, S. K.; Shamsipur, M. MnCoP hollow nanocubes as novel electrode material for asymmetric supercapacitors. *Chem. Eng. J.* **2021**, *420*, 129910.

(21) Li, X.; Elshahawy, A. M.; Guan, C.; Wang, J. Metal phosphides and phosphates-based electrodes for electrochemical supercapacitors. *Small* **2017**, *13*, 1701530.

(22) Li, T.; Kaercher, S.; Roesky, P. W. Synthesis, structure and reactivity of rare-earth metal complexes containing anionic phosphorus ligands. *Chem. Soc. Rev.* **2014**, *43*, 42−57.

(23) Oyama, S. T. Novel catalysts for advanced hydroprocessing: transition metal phosphides. *J. Catal.* **2003**, *216*, 343−352.

(24) Dang, T.; Wei, D.; Zhang, G.; Wang, L.; Li, Q.; Liu, H.; Cao, Z.; Zhang, G.; Duan, H. Homologous NiCoP/CoP hetero-nanosheets supported on N-doped carbon nanotubes for high-rate hybrid supercapacitors. *Electrochim. Acta* **2020**, *341*, 135988.

(25) Mei, Y.; Zhang, H.; Mei, H.; Kang, W.; Xiao, Z.; Zhang, X.; Fan, W.; Xu, B.; Hu, S. Effective preparation of Ni1. 4Co0. 6P@ C micro-spheres with prolonged cycling lives for high performance hybrid supercapacitors. *J. Alloys Compd.* **2020**, *818*, 152828.

(26) Shao, Y.; Zhao, Y.; Li, H.; Xu, C. Three-dimensional hierarchical Ni x Co1−x O/Ni y Co2−y P@ C hybrids on nickel foam for excellent supercapacitors. *ACS Appl. Mater. Interfaces* **2016**, *8*, 35368−35376.

(27) Chen, X.; Li, S.; Liu, Y.; Xie, K.; Wang, Y. MOF-derived Mo-CoP@ NiFe LDH hierarchical nanosheets for high-performance hybrid supercapacitors. *J. Alloys Compd.* **2022**, *919*, 165842.

(28) Isacfranklin, M.; Yuvakkumar, R.; Ravi, G.; Hong, S.; Velauthapillai, D.; Thambidurai, M.; Dang, C.; Algarni, T. S.; Al-Mohaimeed, A. M. Heterostructured SmCoO3/rGO composite for high-energy hybrid supercapacitors. *Carbon* **2021**, *172*, 613−623.

(29) Li, Y.; Zhang, D.; Zhang, Y.; He, J.; Wang, Y.; Wang, K.; Xu, Y.; Li, H.; Wang, Y. Biomass-derived microporous carbon with large micropore size for high-performance supercapacitors. *J. Power Sources* **2020**, *448*, 227396.

(30) Guan, S.; Fu, X.; Zhang, B.; Lei, M.; Peng, Z. Cation-exchange-assisted formation of NiS/SnS 2 porous nanowalls with ultrahigh energy density for battery−supercapacitor hybrid devices. *J. Mater. Chem. A* **2020**, *8*, 3300−3310.

(31) He, P.; Yu, X. Y.; Lou, X. W. Carbon-incorporated nickel−cobalt mixed metal phosphide nanoboxes with enhanced electro-catalytic activity for oxygen evolution. *Angew. Chem.* **2017**, *129*, 3955−3958.

(32) Chen, X.; Wang, D.; Wang, Z.; Zhou, P.; Wu, Z.; Jiang, F. Molybdenum phosphide: a new highly efficient catalyst for the electrochemical hydrogen evolution reaction. *Chemical communica-tions* **2014**, *50*, 11683−11685.

(33) Wu, T.; Pi, M.; Zhang, D.; Chen, S. 3D structured porous CoP 3 nanoneedle arrays as an efficient bifunctional electrocatalyst for the evolution reaction of hydrogen and oxygen. *J. Mater. Chem. A* **2016**, *4*, 14539−14544.

(34) Heidari Gourji, F.; Velauthapillai, D.; Keykhaei, M. Ultra-ordered array of CuCo2S4 microspheres on co-doped nitrogen, sulfur-porous graphene sheets with superior electrochemical performance for supercapacitor application. *Energy Reports* **2022**, *8*, 7712−7723.

(35) Mei, B.-A.; Munteshari, O.; Lau, J.; Dunn, B.; Pilon, L. Physical interpretations of Nyquist plots for EDLC electrodes and devices. *J. Phys. Chem. C* **2018**, *122*, 194−206.

(36) Muchakayala, R.; Song, S.; Wang, J.; Fan, Y.; Bengeppagari, M.; Chen, J.; Tan, M. Development and supercapacitor application of ionic liquid-incorporated gel polymer electrolyte films. *J. Ind. Eng. Chem.* **2018**, *59*, 79−89.

(37) Luo, X.; Shao, J.; He, P.; Zhong, M.; Wang, Q.; Li, K.; Zhao, W. Metal organic framework derived CoS2@ Ni (OH) 2 core-shell structure nanotube arrays for high-performance flexible hybrid supercapacitors. *Electrochim. Acta* **2020**, *354*, 136679.

📖 Recommended by ACS